# Engineering High-Valence Metal-Enriched Cobalt Oxyhydroxide Catalysts for Enhanced OER in Near pH-Neutral Condition

Ruijing Dong[a,b], Jiajian Gao[b], Truong-Giang Vo[b], Shibo Xi[b], Choon Wee Kee[b], Xun Cao[b], Wei Chu[a*], Yan Liu[b*]

[a] School of Chemical Engineering, Sichuan University, No. 24 South Section 1, Yihuan Road, Chengdu, 610065, China.

[b] Institute of Sustainability for Chemicals, Energy and Environment (ISCE$^2$), Agency for Science, Technology, and Research (A*STAR), 1 Pesek Road, Jurong Island, Singapore 627833, Republic of Singapore

[*]Corresponding authors:

chuwei1965@scu.edu.cn (W Chu);

liu_yan@isce2.a-star.edu.sg (Y Liu).

**Abstract**: Understanding water splitting in pH-neutral media has important implications for hydrogen production from seawater. Despite its significance, electrochemical water oxidation and reduction in neutral electrolytes still pose great challenges. This study focuses on designing efficient electrocatalysts capable of promoting oxygen evolution reaction (OER) in neutral media by incorporating high-valence elements into transition metal hydroxides. The optimized two-dimensional Mo-$Co(OH)_2$ nanosheets, which undergo *operando* transformation into oxyhydroxide active species, demonstrated an overpotential of 550 mV at 10 mA $cm^{-2}$ with a Tafel slope of 110.1 mV $dec^{-1}$ in 0.5 M $KHCO_3$. *In situ* X-ray absorption spectroscopy revealed that the incorporation of high-valence elements facilitates the generation of CoOOH active sites at low potential and enhances electron transfer kinetics by altering the electronic environment of the Co center. The study offers new insights for developing more efficient OER electrocatalysts and provides fresh ideas for seawater utilization through the study of reaction mechanism on near pH-neutral OER.

**Keywords**: high-valence elements, near pH-neutral media, oxygen evolution reaction, oxyhydroxides, reaction mechanism, two dimensional nanosheets

# 1. Introduction

Water splitting plays an important role in green hydrogen generation as a $CO_2$-free sustainable fuel under the transformation of the global energy structure within the context of low-carbon economy.[1-3] Electricity-driven water splitting is regarded as an optimal process for hydrogen energy production due to its minimal environmental impact and lack of significant requirements for large-scale, high-risk equipment. Electrolysis of water involves two concurrent semi-reactions: water molecules are reduced at the cathode occurring hydrogen evolution reaction (HER) and water molecules are oxidized at the anode taking place oxygen evolution reaction (OER).[4, 5] However, the slow reaction kinetics of the four-electron transfer mechanism in the OER, as opposed to the two-electron transfer in the HER, limits the wide application of water electrolysis.[6] Transition metal oxides (TMOs) and their hydroxides as catalytic materials were widely studied to improve OER performance due to the advantages of lower costs than noble metals and their magnificent conductivity and stability. For example, Hao et al. studied OER mechanism on NiFe oxyhydroxides using a molecular probe and demonstrated that the chemical O–O coupling step serves as the rate-determining step.[7] Yang et al. developed a novel Co-based NiCoFe LDH exhibited excellent OER performance with 233 mV overpotential.[8] Subsequently, Vo et al. reported a transitional metal-based material Ni-Fe hybrid films which reaching a low overpotential of 316 mV at current density of 10 mA $cm^{-2}$.[9] Charles et al. reported the benchmarking protocol of TMO catalysts for $CoO_x$, CoPi, $CoFeO_x$, $NiO_x$, and $NiCeO_x$ that showed a high OER performance in alkaline solution with overpotentials between 0.35 and 0.43 V.[10]

Furtherly, to improve the intrinsic activity of the transition metal-based catalyst (TMC), doping with high-valence metals (HVMs) into TMCs appears as an effective approach, allowing for control over the local electronic structure and improving the oxidation states of the catalytic active center of TMCs. [11] Meanwhile, HVMs also synergize with TMCs and participate in the OER reaction as the dual active sites. For example, Li et al. demonstrated that Ce-induced reinforcement of the Co–O covalency led a remarkable enhancement in OER performance, achieving an ultra-low overpotential

of 261 mV in 0.1M KOH.[12] Meanwhile, Zhao et al. observed a dual-phase structural transition in bimetallic NiCo-based nanocrystals during the OER process, resulting in abundant oxygen vacancies and high oxidation states formation, which accounted for the high OER activity.[13] Tang et al. observed the potential-dependent formation of OOH* intermediates on chromium (Cr) sites by confining high-valence Cr into a Co oxyhydroxide lattice.[14] Similarly, molybdenum (Mo) played the similar role to Cr, as observed in Mo-CoOOH nanoframes, which exhibited the lowest overpotential of 400 mV and high durability of over 120 hours.[15] These reports indicated that high-valence metals can adjust the microstructure and electronic configuration of transition metals due to HVMs embedding into the TMCs crystal lattice. Additionally, high-valence metals can also serve as adsorption sites for oxygen-containing intermediates such as *OOH, *O, and *OH, thereby further improving the catalytic activity of OER. However, the application of HVMs enhanced TMCs catalysts with high intrinsic activity in near pH-neutral OER has rarely been reported.

Recently, OER in pH-neutral electrolytes has received growing attention.[16-18] One perspective is that neutral dielectrics are necessary for the microbial electrocatalysis system because most microorganisms can only survive under near pH-neutral conditions.[19] Unlike strong acid and alkali solutions, neutral conditions are more environmentally friendly and sustainable. However, despite the environmental advantages, there are challenges associated with OER in near pH-neutral electrolytes. The low solubility of the reactants in the neutral electrolyte limits the OER reaction kinetics, which poses a hurdle in achieving efficient OER.[20] Additionally, the overall reaction pathway for OER in alkaline and neutral solutions differs, indicating potentially different rate-determining steps.[21] Even though the OER pathway in alkaline media (Eq. 1) and neutral media (Eq. 2) are well-established, various perspectives exist in the literature regarding the rate-demining steps. For example, Niu et al. reported formation of OOH* is the rate-determining step, which was accelerated by weakening the adsorption of O on $RuO_2$/$(Co, Mn)_3O_4$.[22] In parallel, Zhong et al. explored $O_2$ production over a cobalt catalyst, revealing that the turnover-limiting chemical step was preceded by a one-electron, one-proton equilibrium in the pH 7.0 electrolyte.[23] Therefore, understanding the OER reaction mechanism

under neutral conditions is important for designing catalysts.[24] Additionally, there is also a pressing need to design an efficient HVOs-enhanced TMC with high intrinsic activity in pH-neutral and understand its reaction mechanism in near pH-neutral media to unlock their full potential in sustainable energy applications using seawater.

$$* + 4OH^- \rightarrow 2H_2O + O_2 + 4e^- \quad (1)$$

$$* + 2H_2O \rightarrow 4\,H^+ + O_2 + 4e^- \quad (2)$$

where * denotes active sites on a catalytic surface

In this work, a series of high-valence metal elements, including Cr (+6), Mo (+6), and W (+6), were modified into the layered $Co(OH)_2$ and their OER activity in near pH-neutral media was investigated. The optimized two-dimensional Mo-$Co(OH)_2$ nanosheets were utilized as a model catalyst to investigate the underlying contributions of incorporating high-valence elements into $Co(OH)_2$ through *in-situ* X-ray absorption analysis and DFT theoretical simulation. Results indicated that the incorporation of Mo beneficially modulated the electronic structure of Co metal hydroxides, facilitating the *operando* formation of CoOOH as the active species in the OER process. Compared to $Co(OH)_2$, the Co-O bond length became shortened in Mo-$Co(OH)_2$, promoting the deprotonation and increasing the valence of Co. This study elucidates the dynamic evolution of active sites and offers guidance for boosting OER performance by incorporating appropriate high-valance metals into transition metal hydroxides.

## 2. Experimental sections

### 2.1 Chemicals

Sodium molybdate dihydrate ($Na_2MoO_4•2H_2O$), Potassium dichromate ($K_2Cr_2O_7$), Sodium tungstate dihydrate ($Na_2WO_4•2H_2O$), Cobalt nitrate hexahydrate ($CoN_2O_6•6H_2O$) Potassium bicarbonate ($KHCO_3$), 2-methylimidazde (MIM) and Nafion (20 wt%) all were bought from Sigma Aldrich. Hexadecyltrimethylammonium bromide (CTAB) was purchased form Alfa Aesar. Ethanol was purchased form VWR CHEMICALS.

## 2.2 Synthesis of 2D nanosheets

High-valence metal-modified $Co(OH)_2$ two-dimensional (2D) nanosheets were synthesized using zeolitic imidazolate frameworks (ZIF67) as a cobalt precursor[15]. In brief, 236 mg of $CoN_2O_6•6H_2O$ and 6.4 mg of CTAB were fully dissolved in 8 ml of deionized water. Subsequently, the solution was swiftly introduced into a 56 ml aqueous MIM solution (3 g) and stirred at ambient temperature for 20 minutes to yield ZIF-67. Centrifuged solid ZIF-67 product was dispersed in ethanol, followed by adding aqueous $Na_2MoO_4$ (280 mg) solution as Mo source. Thereafter, the mixtures were refluxed at 85 °C for 2 h in an oil bath. Centrifugal separation was used to collect the formed Mo-$Co(OH)_2$ and dried at 60 °C after washing with ethanol several times. The synthetic procedure of W-$Co(OH)_2$ and Cr-$Co(OH)_2$ was similar to that of Mo-$Co(OH)_2$, except that $Na_2WO_4$ (272 mg) and $KCrO_7$ (160 mg) were used instead of $Na_2MoO_4$.

## 2.3 Characterization of 2D nanosheets

The crystalline structure of all samples was determined using Powder X-ray diffraction (XRD) analysis conducted on a Bruker D8 Advance X-ray diffractometer, utilizing Cu-Kα radiation (λ = 1.54178 Å) and Bragg–Brentano geometry within the 2θ range of 5-85°. Elemental composition analysis was conducted utilizing inductively coupled plasma-optical emission spectroscopy (ICP-OES) employing an Agilent VISTA-MPX instrument. X-ray photoelectron spectroscopy equipped with an Mg-Kα source (XPS, XSAM800 XPS) was executed to analyze the oxidation state of Co species and all data were calibrated with 284.8 eV of carbon 1s peak. The cubic morphology of ZIF-67 and sheet morphology of prepared samples were evaluated through field emission scanning electron microscopy (FESEM) employing a JSM-6700F instrument. High-resolution transmission electron microscopy coupled with energy-dispersive X-ray spectroscopy (HRTEM/EDX JEM-2100F, 200 kV) was employed for examining the lattice structure and elemental mapping of all samples. The specific surface area of prepared samples was determined via $N_2$ adsorption/desorption isotherms,

calculated using the Brunauer-Emmett-Teller equation (Micromeritics BET ASAP 2420). The X-ray absorption near edge structure (XANES) and extended X-ray absorption fine structure (EXAFS) analyses of the Co K-edge in the samples were conducted using transmission mode at the XAFCA beamline of the Singapore Synchrotron Light Source (SSLS). The SSLS storage ring operated at E = 700 MeV and Imax = 200 mA. Additionally, energy calibration was achieved using Co foil as a reference.

## 2.4 *In situ* X-ray absorption spectroscopy (XAS) process

The *in situ* Co K-edge XAS of $Co(OH)_2$ and Mo-$Co(OH)_2$ was measured at the XAFCA beamline of SSLS within fluorescence mode. Briefly, *in situ* spectroscopic experiments were conducted using a three-electrode system electrochemical Teflon cell, operating under the sensitive fluorescence model. The carbon paper bearing catalyst droplets was affixed to the cell, featuring Ag/AgCl (saturated KCl solution) and Pt wire as reference and counter electrodes, respectively. 0.5 M $KHCO_3$ solution as electrolyte was filled in the cell. Throughout the *in situ* measurement, a range of potentials was applied to the working electrode, which was linked to an electrochemical workstation (Corr Test).

## 2.5 Oxygen evolution reaction Measurements

OER electrochemical tests were performed using an electrochemical workstation (CHI 760E) 0.5M $KHCO_3$ solution (pH = 8.5) served as the electrolyte, with Pt mesh employed as the counter electrode, and Ag/AgCl (saturated KCl solution, $E_{RHE} = E_{Ag/AgCl} + 0.059*pH + 0.197$) utilized as the reference electrode. The working electrode, composed of glassy carbon with a geometric area of 0.196 $cm^2$, was loaded with various catalysts. Normally, to achieve a uniform ink, 2 mg of electrocatalyst and 6.25 μl of Nafion were added to 1 ml of ethanol, followed by ultrasonic dispersion. Subsequently, 20 μL of the ink was deposited onto the surface of a glassy carbon electrode via drop-casting and dried under an infrared lamp. The electrochemical measurements were performed utilizing a rotating

disk electrode (RDE) at 25°C, employing a scan rate of 5 mV $s^{-1}$ at 1600 rpm. Prior to the linear sweep voltammetry (LSV) test, the catalysts underwent repeated sweeps from 1.2 V to 1.9 V (vs. RHE) in a 0.5 M $KHCO_3$ solution until a stable voltammogram curve was achieved.

OER performance was investigated by LSV, which were obtained by using automatic iR (i, current; R, resistance) correction (100%) of the workstation. Electrochemical impedance spectroscopy (EIS) was conducted within a frequency range spanning from 100,000 Hz to 0.01 Hz, while maintaining a potential of 1.8 V (vs. RHE). The double-layer capacitance ($C_{dl}$) was calculated using cyclic voltammetry (CV) under different scan rates from 5 to 25 mV $s^{-1}$. Stability test of $Co(OH)_2$ and Mo-$Co(OH)_2$ using chronoamperometry, with the potential maintained at 10 mA $cm^{-2}$, as determined from the LSV profile.

## 2.6 Theoretical simulation details

Theoretical simulations were conducted using density-functional theory (DFT) analysis. Spin-polarized calculations were executed using version 6.4.2 of the Vienna Ab initio Simulation Package (VASP), employing projector-augmented-wave pseudopotentials.[25-28] The Perdew-Burke-Ernzerhof generalized gradient approximation functional was selected as the density functional theory (DFT) functional. High precision mode (PREC=accurate) was utilized with a plane-waves' energy cut-off of 800 eV and an augmentation charge cut-off of 1000 eV. The convergence criterion for electronic energy was set to $10^{-8}$ eV. A Gaussian smearing of 0.05 width was applied in the self-consistent field calculation. The Brillouin zone integration was achieved by sampling a Gamma-centered k-point mesh with a spacing of 0.5 $Å^{-1}$, generated automatically through the "KSPACING" keyword. Dispersion interactions were considered using the D3 method with Becke-Jonson damping.[29] For ionic relaxation, the convergence criteria is such that the norms of all the force is less than 0.01 eV/Å. Numerical integration is done via the finite differences approach. The width of the displacement of each ion is set to 0.01 Å. Thermochemical corrections to the Gibbs free energy are calculated with VASPKIT.[30]

## 3. Results and Discussion

### 3.1 Synthesis and Characterization of HVM-modified $Co(OH)_2$ two dimensional (2D) nanosheets

High-valence metal-modified $Co(OH)_2$ 2D nanosheets were synthesized by introducing HVMs into cobalt hydroxides, utilizing ZIF-67 cubes as a growth template. Upon addition of the Mo source into ZIF-67 dispersion, with subsequent heating and refluxing, the ZIF-67 cube was transformed into $Co(OH)_2$ double layered hydroxides. Concurrently, the $MoO_4^{2-}$ intercalated within the layers of $Co(OH)_2$ , resulting in the formation of nanosheets denoted as Mo-$Co(OH)_2$. Similarly, Cr-$Co(OH)_2$ and W-$Co(OH)_2$ were prepared using Cr source and W source instead of Mo. Fig. 1(a) shows SEM images of ZIF-67, revealing their nanocubic morphology with an average size of 300 nm. The XRD pattern of ZIF-67 was indicated in Fig 1(b), with 2θ at 7º, 10.2º, 12.5º, 34.5º, 14.5º, 16º, 18º, 22º, 24.3º, 26.5º, corresponding to ZIF-67 planes of (011), (002), (112), (022), (013), (222), (114), (223), and (134), respectively. XRD pattern of HVM-$Co(OH)_2$ 2D nanosheets was shown in Fig 1(c), all significant peaks corresponding to α-$Co(OH)_2$, which has a larger distance between layers than that for β-$Co(OH)_2$. Larger layer spacing offered a convenience for mass transfer and HVMs ion insertion.[31] The 2θ peak at 11.6º, 23.2º, 33.5º, 34.5º, 60º corresponds to (003), (006), (012), (100), and (110) plane of cobalt hydroxides (JCPDS No. 46-0605).[32] There were no striking distinctions in the crystal structure by introducing different high valence metals, which demonstrates the preservation of α-$Co(OH)_2$ structure. Fig. 1(d)-(f) displays the nanosheet-shaped morphology of Mo-$Co(OH)_2$, Cr-$Co(OH)_2$, and W-$Co(OH)_2$, respectively, as observed via high-resolution TEM (HRTEM). No separate particles of HVMs were observed, further suggesting the preservation of the original structure of α-$Co(OH)_2$. Results also illustrate the versatility and wide applicability of the synthesis method due to its simplicity. The elemental mapping depicted in Fig. 1(g) and Fig. S2 illustrates Co and Mo (or Cr or W) elements were evenly dispersed on the nanosheets, proposing that the successful incorporation of HVMs into $Co(OH)_2$.

Measured from HRTEM image of Mo-$Co(OH)_2$ (Fig. 1h), the lattice spacing of 0.25 nm reveals the existence of (110) plane of crystalline $Co(OH)_2$. Additionally, the selected area electron diffraction pattern depicted in Fig. 1(i) shows a good polycrystalline structure, with (006), (100), and (110) diffraction planes of $Co(OH)_2$ aligning closely those observed in the XRD.[33] The specific surface area of Mo-$Co(OH)_2$, Cr-$Co(OH)_2$ and W-$Co(OH)_2$, as measured by using $N_2$ adsorption/desorption isotherms (Fig. S3), were 137.1 $m^2$ $g^{-1}$, 234.8 $m^2$ $g^{-1}$, and 172.1 $m^2$ $g^{-1}$, respectively, implying that high specific surface area catalysts could be effectively obtained through a simple hydrolysis method.

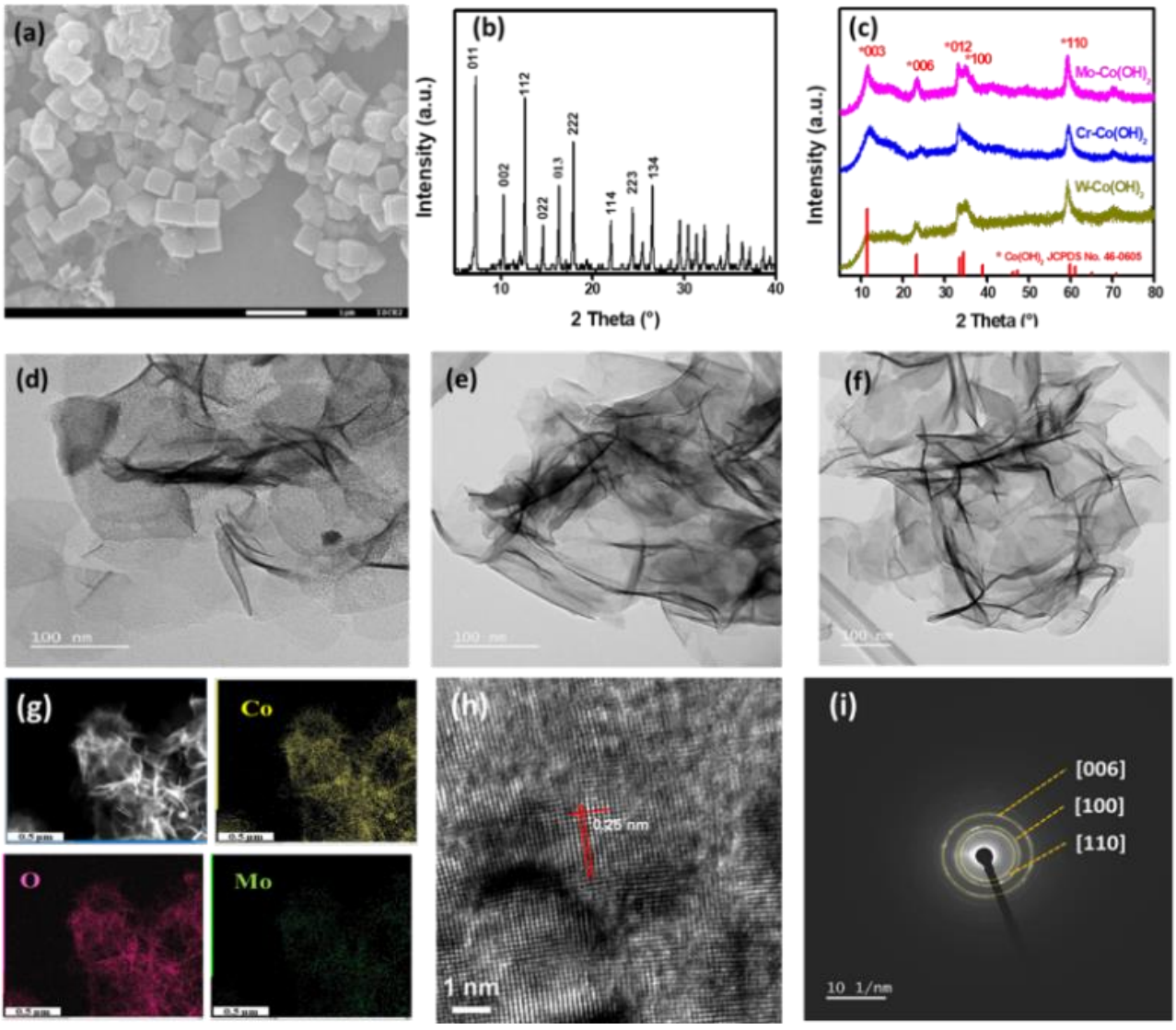


Fig. 1 The SEM image (a) and XRD pattern (b) of ZIF-67 template. XRD pattern of Mo-$Co(OH)_2$, Cr-$Co(OH)_2$ and W-$Co(OH)_2$ (c). TEM image of Mo-$Co(OH)_2$, Cr-$Co(OH)_2$ and W-$Co(OH)_2$ 2D

nanosheets (d)~(f). TEM mapping images of Mo-$Co(OH)_2$ (g). High-resolution TEM (HRTEM) image of Mo-$Co(OH)_2$ (h) and selected area electron diffraction pattern of Mo-$Co(OH)_2$ (i)

## 3.2 Electrocatalytic Oxygen Evolution performance of HVM-modified $Co(OH)_2$

The OER performance was investigated using LSV in a 0.5 M $KHCO_3$ solution (pH 8.5). Figure 2(a) shows that electrocatalytic ability of HVM-modified $Co(OH)_2$ is significantly superior to that of the unmodified $Co(OH)_2$, indicating the enhancing effect of HVM on the OER. Among the samples tested, Mo-$Co(OH)_2$ emerges as the most effective OER catalyst, exhibiting the highest current density at a given overpotential. Specifically, to achieve a current density of 10 mA $cm^{-2}$, the Mo-$Co(OH)_2$ gave an overpotential of 550 mV. This value is notably lower compared to Cr-$Co(OH)_2$ (570 mV) and W-$Co(OH)_2$ (640 mV). Except for pure $Co(OH)_2$ sample, the anodic wave corresponding to a transformation of $Co(OH)_2$ to CoOOH, being as the activity sites during the OER reaction, as clearly observed in the LSV curve.[34, 35] The introduction of HVMs allowed the generation of CoOOH at a lower voltage. Results demonstrated HVMs promoting the charge transfer, thereby facilitating the efficient removal of protons in the initial step of the OER process because of strong covalency of M–O interaction.[36] It is noteworthy that an excessively strong electronic interaction between HVM and Co might impede the oxidation of $Co^{2+}$ to a certain extent, as evidenced by the positive shift observed in the anodic wave of $Co^{2+}/Co^{3+}$ from Cr-$Co(OH)_2$ to W- $Co(OH)_2$. In general, the electrocatalytic ability of $Co(OH)_2$ was promoted by the incorporation of HVMs.

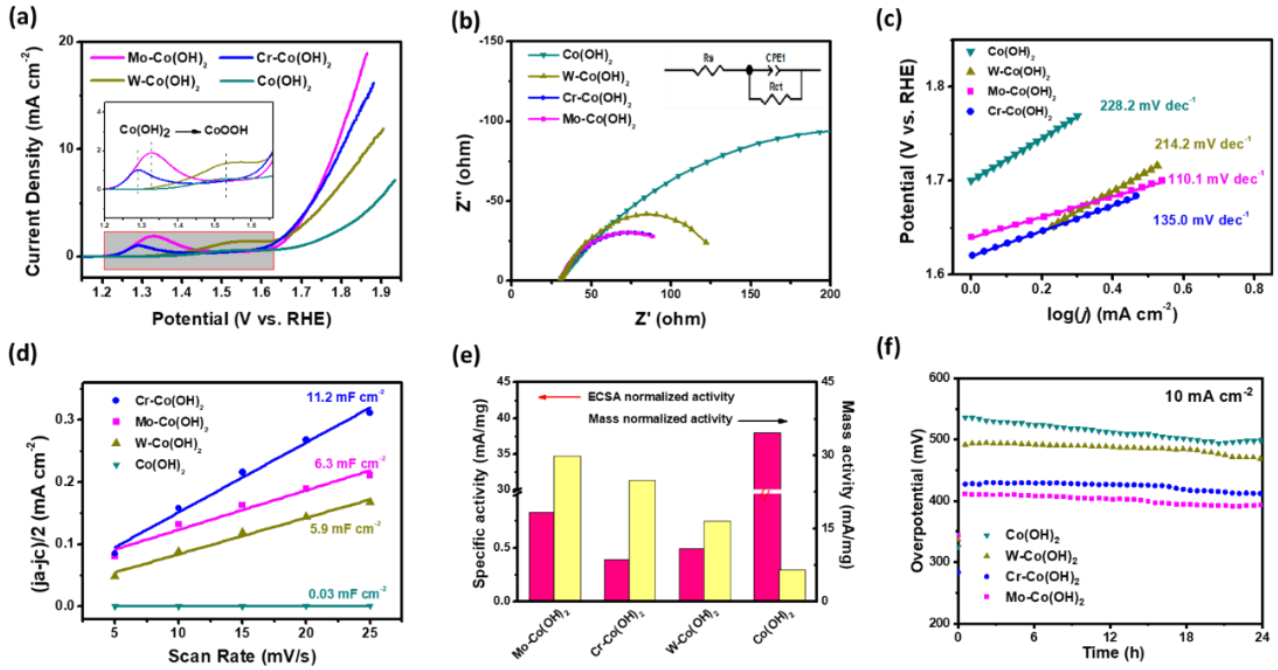


Fig 2. iR-corrected polarization curves of HVM-modified $Co(OH)_2$ for OER (a) . Nyquist plots and the inset show the equivalent circuit mode (b). Tafel slope plots for different catalysts (c). Double-layer capacitance plots of different catalysts (d). The specific activity was normalized by ECSA and Mass (e) and stability test of $Co(OH)_2$ and HVM-modified $Co(OH)_2$ under 10 mA cm-$^{-2}$ (f)

Electrochemical Impedance Spectroscopy (EIS) was carried out to investigate the charge-transfer processes and electrode kinetic. The corresponding Nyquist plot is depicted in Fig. 2(b), with the inset showcasing the equivalent circuit used for analysis. The solution resistance ($R_s$), which includes electrode resistance itself, was close, implying the similar conductivity for Mo-$Co(OH)_2$, Cr-$Co(OH)_2$ and W-$Co(OH)_2$. The fitted charge transfer resistances ($R_{ct}$) were 118.96 Ω of Mo-$Co(OH)_2$, 112.61 Ω of Cr-$Co(OH)_2$, and 136.2 Ω of W-$Co(OH)_2$, respectively, all of which were lower than that of $Co(OH)_2$ (389 Ω). It suggested that compared to pure $Co(OH)_2$, the incorporation of high-valence elements into $Co(OH)_2$ resulted in faster electron transfer kinetics. The optimized electronic structure and charge conductivity benefits the enhancement of OER performance.[37] In Fig. 2(c), the Tafel slope value of Mo-$Co(OH)_2$ was 110.1 mV dec$^{-1}$, demonstrating faster kinetics of Mo-$Co(OH)_2$ compared to Cr-$Co(OH)_2$ (135.0 mV dec$^{-1}$) and W-$Co(OH)_2$ (214.2 mV dec$^{-1}$) and $Co(OH)_2$ (228.2 mV dec$^{-1}$). The electrochemically active surface area (ECSA) was calculated using Eq. (3) for

all samples, where the double-layer capacitance ($C_{dl}$) was acquired from cyclic voltammetry (CV) at different scan rates (Fig. S4) and the specific capacitance ($C_s$) of 40 μF $cm^{-2}$.[38, 39]

$$ECSA = \frac{C_{dl}}{C_s} \quad (3)$$

As shown in Fig. 2(d), there was a distinct difference between different catalysts; the $C_{dl}$ of Cr-$Co(OH)_2$ was a maximum of 11.2 mF $cm^{-2}$ compared with 6.3 mF $cm^{-2}$ of Mo-$Co(OH)_2$ and 5.9 mF $cm^{-2}$ of W-$Co(OH)_2$. Results propose that all HVM-modified $Co(OH)_2$ could provide more active sites and possess higher ECSA (Table S1). In Fig. 2(e), the ECSA normalized activity and mass normalized activity revealed that Mo-$Co(OH)_2$ had the greatest specific activity. Stability testing at 10 mA $cm^{-2}$ was depicted in Fig. 2f. There is no significant decrease in the activity of $Co(OH)_2$ and all HVM-modified $Co(OH)_2$ within 24 hours. Among them, Mo-$Co(OH)_2$ gives the lowest overpotential at 390 mV at a current density of 10 mA $cm^{-2}$. Therefore, Mo-$Co(OH)_2$ would be the example of HVMs enhanced cobalt oxyhydroxide to investigate the microstructures and understand the catalytic mechanism in the following parts.

## 3.3 Surface chemistry and local environment of Mo-CoOOH Nanosheets

The element valence and chemical contents of Mo-$Co(OH)_2$ and $Co(OH)_2$ were analyzed using X-ray photoelectron spectroscopy (XPS). As shown in Fig. 3(a), the peak-fitting of 781.4 eV and 796.9 eV corresponding to $2p_{3/2}$ and $2p_{1/2}$ orbital of $Co^{2+}$, there was no distinct difference in Co chemical states between the pristine and HVM-modified $Co(OH)_2$.[40] However, compared with pristine Mo-$Co(OH)_2$, the binding energy of $Co^{2+}$ has shifted to a higher around 0.4 eV after OER, being 780.35 eV and 795.8 eV corresponding to $2p_{3/2}$ and $2p_{1/2}$ orbital of $Co^{3+}$ in Mo-$Co(OH)_2$ after OER process. Results suggested that high valence Mo would promote the oxidation of Co species, due to a strong covalent between Mo and Co.[41] The XPS peak-fitting analysis substantiated the increase of the valence state of Co species facilitated by Mo, thereby promoting the formation of CoOOH as an active site in OER at a relatively lower potential. The result is consistent with the observed OER performance (Fig. 2). The electronic environment of the catalytic active center would

be optimized by introducing HVMs, thus improving the intrinsic activity cobalt-based catalysts. As shown in Fig. S6, the nanosheets 2D morphology of the HVM-modified $Co(OH)_2$ is well maintained after OER process.

To further investigate the impact of HVMs on the coordination environment of TMCs, X-ray absorption fine structure (XAFS) spectroscopy are conducted for Mo-$Co(OH)_2$ and $Co(OH)_2$ catalysts. In Fig. 3(b), X-ray near-edge absorption fine structure (XANES) showed similar absorption energy of 7718 eV at Co K-edge, which demonstrated identical initial chemical states of Co species in Mo-$Co(OH)_2$ and $Co(OH)_2$, being consistent with XPS conclusion. Compared with $Co(OH)_2$, the white line of Co K-edge in Mo-$Co(OH)_2$ was slightly weaker, indicating the 4p orbital splitting of Co is getting greater.[42] This phenomenon results in the spin state or symmetry properties of Co being changed by incorporating high-valence of Mo.[43]

Fig. 3(c), i.e. the Fourier transform (FT) of Co K-edge extended XAFS (EXAFS) of Co foil, shows a dominating peak of Co-Co at 2.49 Å. $Co(OH)_2$ exhibited the Co-O peak at 2.09 Å and Co-Co peak at 3.19 Å, which all shift to a lower R in Mo-$Co(OH)_2$ (i.e. Co-O peak at 2.06 Å and Co-Co/Mo peak at 3.13 Å). Simulation of quantitative structural parameters of Co atoms in Mo-$Co(OH)_2$ by least-squares EXAFS curve fit, where the Co–O coordination number was about 5.1 in Mo-$Co(OH)_2$ and distinguished from the standard coordination number of 6 in $Co(OH)_2$ (Table S2), suggesting that cationic vacancy exists.[44]

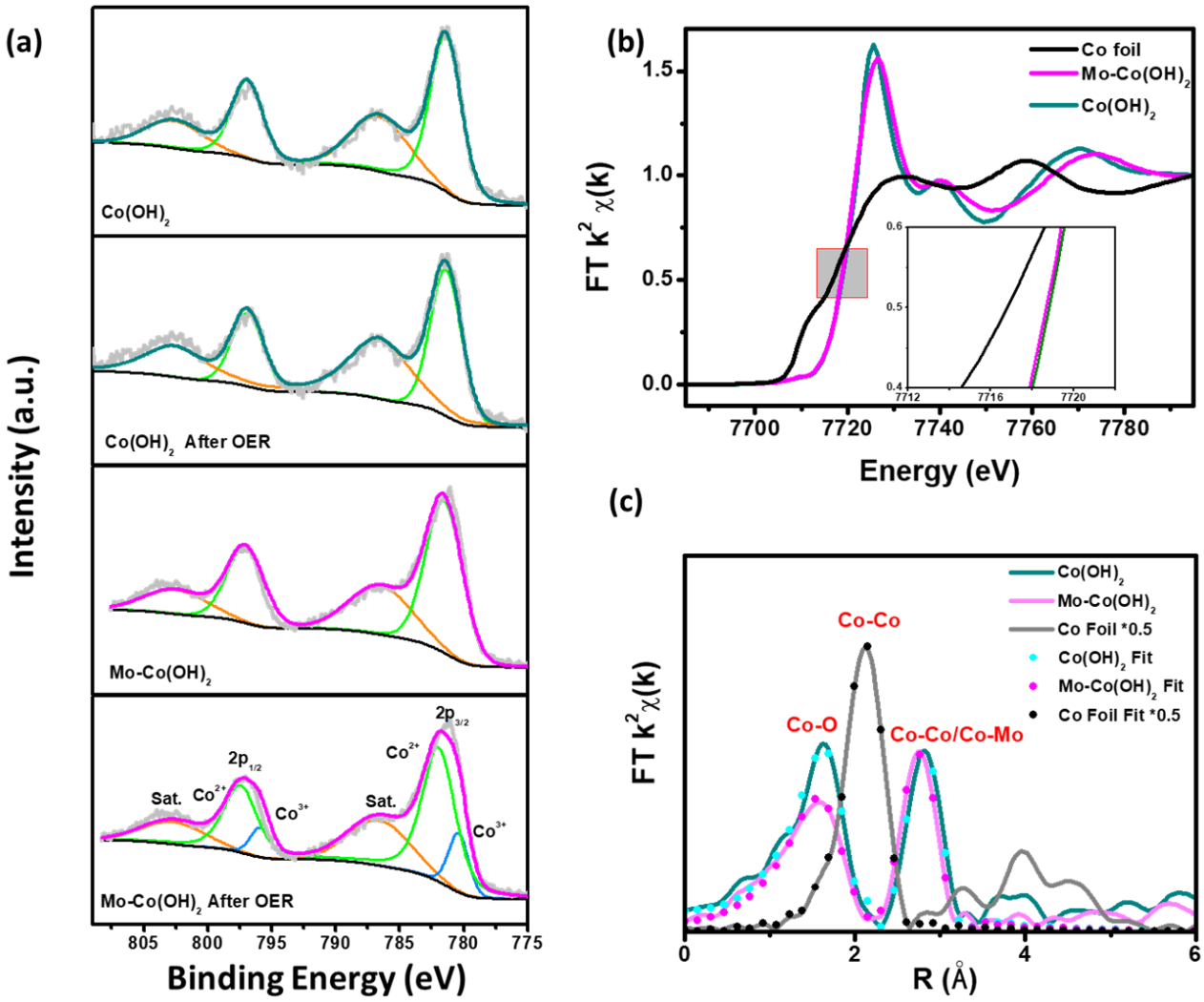


Fig. 3 XPS absorption spectra of Co 2p for the Mo-$Co(OH)_2$ and $Co(OH)_2$ (a), Co K-edge XAFS absorption spectra of Mo-$Co(OH)_2$, $Co(OH)_2$ and Co foil (b) and k2-weighted Fourier transformation of the Co K-edge EXAFS absorption spectra

## 3.4 In-situ/operando XAS studies for understanding catalysis mechanism

Operando XAS analysis was utilized to elucidate the potential catalytic mechanism by investigating dynamic changes in the oxidation state of Co under OER-relevant potentials. Fig. 4(a) and 4(d) displayed the operando XANES spectra at the Co K-edge of the $Co(OH)_2$ and Mo-$Co(OH)_2$ recorded at different applied potentials. From open circuit potential (OCP) to 1.5 V, the Co absorption edge was shifted to a higher energy, showing an increased Co oxidation state. The weakened and broadened white line peak of the Co K-edge in Mo-$Co(OH)_2$ with increased potential suggests the molecular orbital formation due to Mo d orbital hybridized with the Co p orbital.[36] Compared with

the wavelet transformed of the k2-weighted EXAFS (WTEXAFS) signals of Co K-edge of $Co(OH)_2$ (Fig. 4b) and Mo-$Co(OH)_2$ (Fig. 4e) at 1.4 V, the intensity of Co−M in Mo-$Co(OH)_2$ was stronger than that of $Co(OH)_2$, suggesting that atomic Mo have been successfully modified in $Co(OH)_2$. Moreover, when comparing the WTEXAFS signals of Co K-edge of $Co(OH)_2$ (Fig. 4c) and Mo-$Co(OH)_2$ (Fig. 4f) at 1.7 V, the intensity of Co−O in Mo-$Co(OH)_2$ was stronger than that of $Co(OH)_2$, further demonstrating that the introduction of Mo promoting the oxidation of Co species, being consistent with findings from XPS analysis. Fig. 4(g) indicates a schematic operando oxidation process of $Co(OH)_2$ to CoOOH during OER. It suggests that $Co(OH)_2$ undergoes the first deprotonation step at a higher voltage (1.7 V) compared with Mo-enhanced $Co(OH)_2$ of 1.5 V. According to the previous analysis, the radius of Co-O shifted downward, and the electronic environment of Co center were regulated by the incorporation of Mo, thereby showing a better OER intrinsic activity of Mo-$Co(OH)_2$.

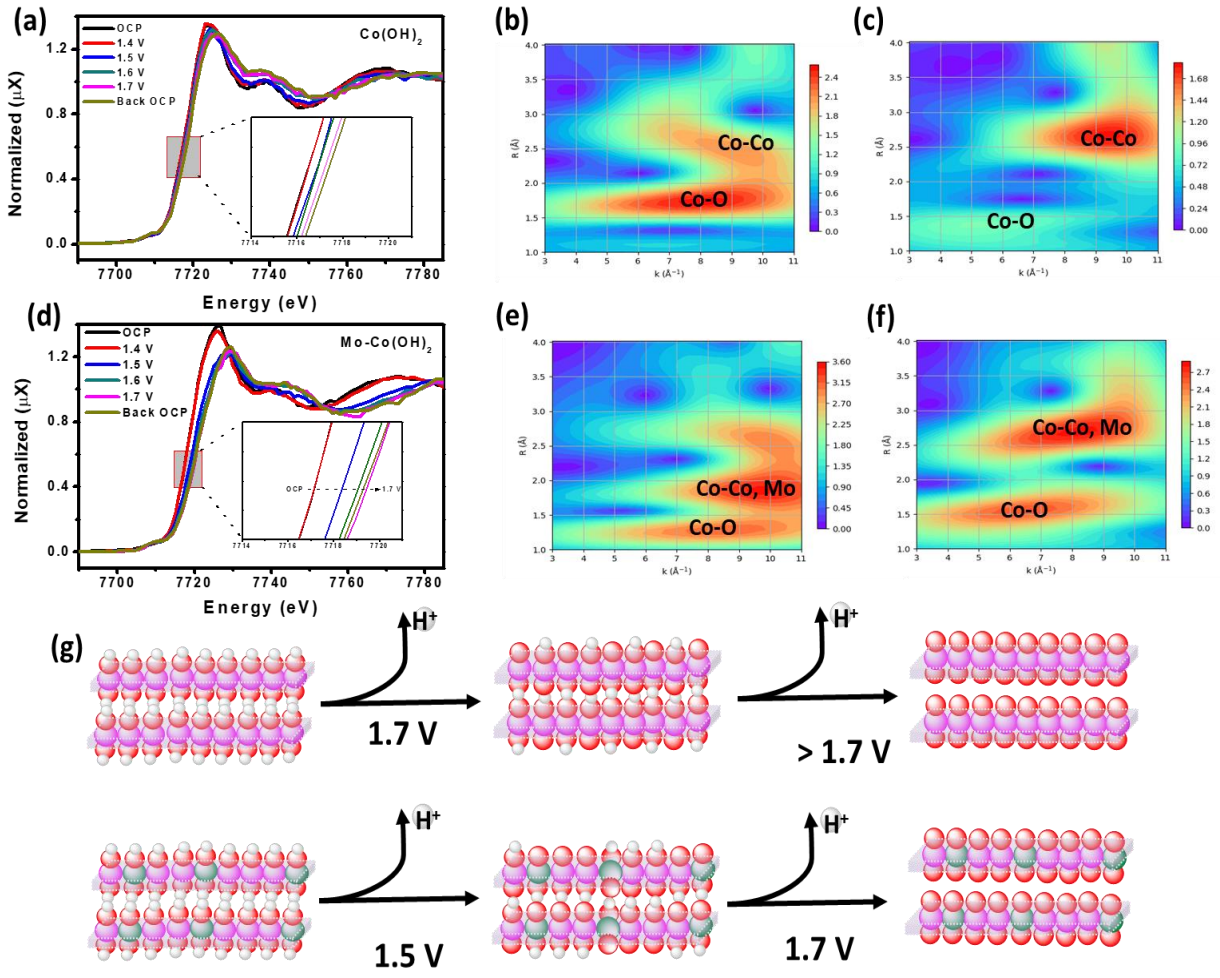

Fig. 4 Operando XAFS Co K-edge absorption spectra of $Co(OH)_2$ (a), Wavelet transformation of the k2-weighted Co K-edge absorption EXAFS signals of $Co(OH)_2$ at 1.4 V (b) and 1.7 V(c), operando XAFS Co K-edge absorption spectra of Mo-$Co(OH)_2$ (d), Wavelet transformation of the k2-weighted Co K-edge absorption EXAFS signals of Mo-$Co(OH)_2$ at 1.4 V (e) and 1.7 V (f). Schematic oxidation process of $Co(OH)_2$ to CoOOH during OER (g): O (red), H (white), Co (purple), Mo(green).

## 3.5 Mechanism Analysis

The theoretical OER mechanism analysis was carried out using Density Functional Theory (DFT) calculations. The thermodynamics for the OER according to the following electrochemical steps are calculated:

$$* + H_2O \rightarrow *OH + H+ + e- \quad (4)$$

$$*OH \rightarrow *O + H+ + e- \quad (5)$$

$$*O + H_2O \rightarrow *OOH + H+ + e- \quad (6)$$

$$*OOH \rightarrow O_2* + H+ + e- \quad (7)$$

$$O_2* \rightarrow O_2\,(g) + * \quad (8)$$

The Computational Hydrogen Electrode Model was utilized to compute the free energy diagram for the OER reaction (Fig. 5a).[45, 46] The fully oxidized form of Mo-CoOOH – Mo-$CoO_2$ – was used as the model as reported by Tang et al.[15] However, the ratio of Mo to Co in our model is 1 to 8 to reflect the stoichiometry more closely as determined from ICP-OES results. Consistent with the result of Tang et al., the adsorption of OH does not take place if the ionic relaxation is initiated with the OH on top of the Co atoms, but it occurs on the Mo atom. The limiting potential of Mo-CoOO in the neutral OER is +1.57 V. The probable rate-determining step for the OER is *O + OH to *OOH with a barrier of at least 0.34 V.

We observed the similar barrier energy with *OOH formation, *OH formation (Eq. 4) at least 0.31 V and the barrier energy of *O formation (Eq. 5) at least 0.24 V, demonstrating the first three steps limited OER at thermodynamics. From the Tafel slope investigation shown in Fig. 2(c), the

*OH formation (Eq. 4) extremely limited OER at kinetics within a low reaction rate. Overall, combined DFT conclusion in thermodynamics with Tafel slope results in kinetics the rate-determining step of OER in pH-neutral electrolytes on HVMs-enhanced CoOOH was the adsorption and dissociation of $H_2O$ which is *OH formation.

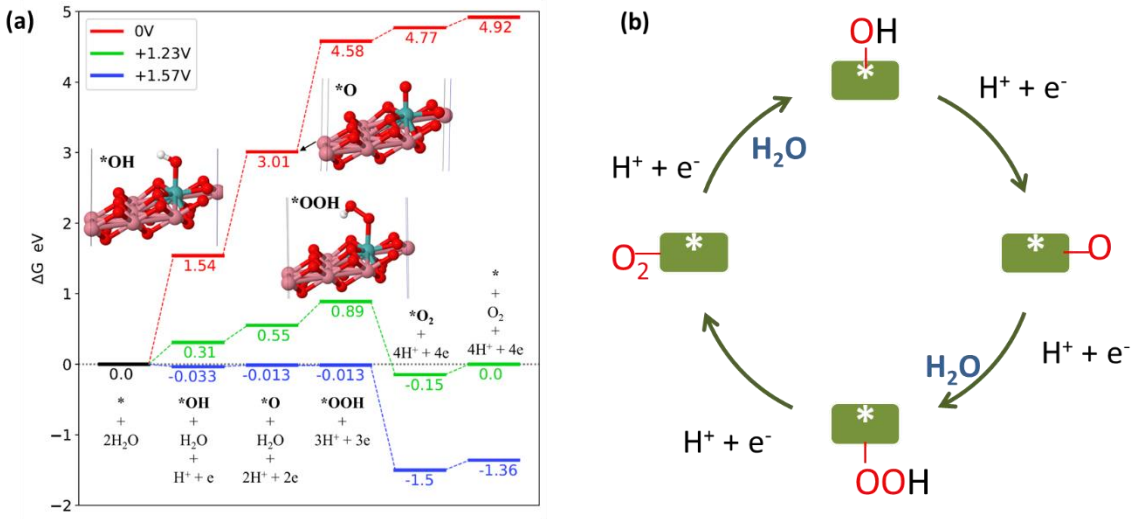


Fig. 5. Free Energy Diagram (a) of OER catalysed by Mo-$CoO_2$ at 0 V (red), +1.23 V (green) and +1.57 V (blue) electrode potential. Schematic OER mechanism on Mo-$Co(OH)_2$ (b)

Fig. 5(b) shown a schematic OER pathway on Mo-$Co(OH)_2$ according to the traditional adsorbate evolution mechanism. Coupled with a four-electron transfer process of OER, molecular $H_2O$ was adsorbed on the catalyst surface, initially forming *OH by removing one proton and one electron. Further, the deprotonation of *OH generates *O, which combines with another $H_2O$ to form intermediate *OOH. The final step was the removal of the proton and electron of *OOH together with the desorption of $O_2$. The adsorbate evolution mechanism indicated that O atoms of $O_2$ originate from $H_2O$ instead of lattice O of catalysts.[47, 48]

## 4. Conclusion

In summary, a comprehensive investigation on a series of high-valence element modified $Co(OH)_2$ two-dimensional nanosheets development and their OER electrocatalytic performance was successfully conducted. Among all investigated samples, Mo-$Co(OH)_2$ emerged as the most efficient

OER catalyst in near pH-neutral media. Subsequent *in situ* XAS analysis revealed that incorporating of HVMs was beneficial for the *operando* generation of CoOOH active sites at a low overpotential during OER process. In the near pH-neutral media, there are two aspects to be considered for further improving their catalytic performance. One is to promote the adsorption and dissociation of $H_2O$, while the other is to enhance the formation of *OOH and *O intermediate. These findings provide new insights for developing more efficient OER electrocatalysts under near pH-neutral condition, understanding their active species evolution, and providing new ideas in seawater utilization for green hydrogen production, etc.

## CRediT authorship contribution statement

**Ruijing Dong**: conceptualization, investigation and manuscript preparation. **Jiajian Gao**: results discussion and manuscript revision. **Truong-Giang Vo**: Electrochemical testing discussion, analysis and manuscript revision. **Shibo Xi**: XAS analysis and data interpretation; **Choon Wee Kee**: DFT simulation and mechanism discussion. **Xun Cao**: HRTEM analysis and data interpretation; **Wei CHU**: supervision, manuscript revision. **Yan LIU**: supervision, formal analysis, manuscript revision, funding acquisition.

## Conflicts of interest

The authors declare that they have no known competing financial interests or personal relationships that could appear to influence the work reported in this paper.

## Acknowledgments

The authors appreciate the Chinese Scholarship Council (CSC) for providing the Ph. D. scholarship and ISCE$^2$ (A-STAR, Singapore) for the financial support. This research is supported by the National Research Foundation, Singapore, and PUB, Singapore's National Water Agency under its Competitive Funding for Water Research (CWR-2101-0029). The computational work for this article was partially performed on resources of the National Supercomputing Centre, Singapore (https://www.nscc.sg). This work was also supported by the A*STAR Computational Resource Centre through its high-performance computing facilities. Authors gratefully acknowledge Ms. Wang Zhan April, Ms. Zheng Jia E and Mr. Yeo Wen Cong (ISCE$^2$, A*STAR, Singapore) for their assistance with XPS, ICP and BET tests, respectively.

## References


1. P. Hota, A. Das and D. K. Maiti, *International Journal of Hydrogen Energy*, 2023, **48**, 523-541.
2. J. Guo, Y. Zhang, A. Zavabeti, K. Chen, Y. Guo, G. Hu, X. Fan and G. K. Li, *Nat Commun*, 2022, **13**, 5046.
3. D. E. H. J. Gernaat, H. S. de Boer, V. Daioglou, S. G. Yalew, C. Müller and D. P. van Vuuren, *Nature Climate Change*, 2021, **11**, 119-125.
4. Y. P. Zhu, C. Guo, Y. Zheng and S. Z. Qiao, *Acc Chem Res*, 2017, **50**, 915-923.
5. M. G. Walter, E. L. Warren, J. R. McKone, S. W. Boettcher, Q. Mi, E. A. Santori and N. S. Lewis, *Chem Rev*, 2010, **110**, 6446-6473.
6. J. Song, C. Wei, Z. F. Huang, C. Liu, L. Zeng, X. Wang and Z. J. Xu, *Chem Soc Rev*, 2020, **49**, 2196-2214.
7. Y. Hao, Y. Li, J. Wu, L. Meng, J. Wang, C. Jia, T. Liu, X. Yang, Z. P. Liu and M. Gong, *J Am Chem Soc*, 2021, **143**, 1493-1502.
8. Q. Yang, T. Li, Z. Lu, X. Sun and J. Liu, *Nanoscale*, 2014, **6**, 11789-11794.
9. T. G. Vo, S. D. S. Hidalgo and C. Y. Chiang, *Dalton Trans*, 2019, **48**, 14748-14757.
10. C. C. McCrory, S. Jung, J. C. Peters and T. F. Jaramillo, *J Am Chem Soc*, 2013, **135**, 16977-16987.
11. H. Wang, T. Zhai, Y. Wu, T. Zhou, B. Zhou, C. Shang and Z. Guo, *Adv Sci (Weinh)*, 2023, **10**, e2301706.
12. M. Li, X. Wang, K. Liu, H. Sun, D. Sun, K. Huang, Y. Tang, W. Xing, H. Li and G. Fu, *Adv Mater*, 2023, **35**, e2302462.
13. S. Zhao, C. Tan, C.-T. He, P. An, F. Xie, S. Jiang, Y. Zhu, K.-H. Wu, B. Zhang, H. Li, J. Zhang, Y. Chen, S. Liu, J. Dong and Z. Tang, *Nature Energy*, 2020, **5**, 881-890.
14. L. Tang, M. Xia, S. Cao, X. Bo, S. Zhang, Y. Zhang, X. Liu, L. Zhang, L. Yu and D. Deng, *Nano Energy*, 2022, **101**.

15. L. Tang, L. Yu, C. Ma, Y. Song, Y. Tu, Y. Zhang, X. Bo and D. Deng, *Journal of Materials Chemistry A*, 2022, **10**, 6242-6250.
16. Y. Jiao, Y. Zheng, M. Jaroniec and S. Z. Qiao, *Chem Soc Rev*, 2015, **44**, 2060-2086.
17. L. Q. Zhou, C. Ling, H. Zhou, X. Wang, J. Liao, G. K. Reddy, L. Deng, T. C. Peck, R. Zhang, M. S. Whittingham, C. Wang, C. W. Chu, Y. Yao and H. Jia, *Nat Commun*, 2019, **10**, 4081.
18. L. Zhang, L. Wang, Y. Wen, F. Ni, B. Zhang and H. Peng, *Adv Mater*, 2020, **32**, e2002297.
19. C. Liu, B. C. Colon, M. Ziesack, P. A. Silver and D. G. Nocera, *Science*, 2016, **352**, 1210-1213.
20. K. Xu, H. Cheng, L. Liu, H. Lv, X. Wu, C. Wu and Y. Xie, *Nano Lett*, 2017, **17**, 578-583.
21. I. C. Man, H. Y. Su, F. Calle‐Vallejo, H. A. Hansen, J. I. Martínez, N. G. Inoglu, J. Kitchin, T. F. Jaramillo, J. K. Nørskov and J. Rossmeisl, *ChemCatChem*, 2011, **3**, 1159-1165.
22. S. Niu, X.-P. Kong, S. Li, Y. Zhang, J. Wu, W. Zhao and P. Xu, *Applied Catalysis B: Environmental*, 2021, **297**.
23. D. K. Zhong and D. R. Gamelin, *J Am Chem Soc*, 2010, **132**, 4202-4207.
24. J. Gao, H. Tao and B. Liu, *Adv Mater*, 2021, **33**, e2003786.
25. G. Kresse and J. Furthmuller, *Phys Rev B Condens Matter*, 1996, **54**, 11169-11186.
26. G. Kresse and J. Furthmüller, *Computational Materials Science*, 1996, **6**, 15-50.
27. G. Kresse and J. Hafner, *Phys Rev B Condens Matter*, 1993, **47**, 558-561.
28. G. Kresse and D. Joubert, *Physical Review B*, 1999, **59**, 1758-1775.
29. S. Grimme, S. Ehrlich and L. Goerigk, *J Comput Chem*, 2011, **32**, 1456-1465.
30. V. Wang, N. Xu, J.-C. Liu, G. Tang and W.-T. Geng, *Computer Physics Communications*, 2021, **267**.
31. N. P. Dileep, T. V. Vineesh, P. V. Sarma, M. V. Chalil, C. S. Prasad and M. M. Shaijumon, *ACS Applied Energy Materials*, 2020, **3**, 1461-1467.
32. R. Jia, M. Xia, L. Tang, L. Yu, Y. Yang, Y. Zhang, X. Bo, S. Zhou, Y. Tu and D. Deng, *ACS Catalysis*, 2022, **12**, 13513-13522.

33. J. Zhao, Z. Huang, J. Zeng, M. Deng, G. Yin, X. Liao and J. Gu, *Journal of Inorganic and Organometallic Polymers and Materials*, 2011, **22**, 492-499.

34. T.-G. Vo, P.-Y. Ho and C.-Y. Chiang, *Applied Catalysis B: Environmental*, 2022, **300**.

35. S. Wang, Q. Jiang, S. Ju, C. S. Hsu, H. M. Chen, D. Zhang and F. Song, *Nat Commun*, 2022, **13**, 6650.

36. J. Suntivich, K. J. May, H. A. Gasteiger, J. B. Goodenough and Y. Shao-Horn, *Science*, 2011, **334**, 1383-1385.

37. N. T. Suen, S. F. Hung, Q. Quan, N. Zhang, Y. J. Xu and H. M. Chen, *Chem Soc Rev*, 2017, **46**, 337-365.

38. A. Moysiadou, S. Lee, C. S. Hsu, H. M. Chen and X. Hu, *J Am Chem Soc*, 2020, **142**, 11901-11914.

39. S. Jung, C. C. L. McCrory, I. M. Ferrer, J. C. Peters and T. F. Jaramillo, *Journal of Materials Chemistry A*, 2016, **4**, 3068-3076.

40. S. L. Zhang, B. Y. Guan, X. F. Lu, S. Xi, Y. Du and X. W. D. Lou, *Adv Mater*, 2020, **32**, e2002235.

41. X.-Z. Song, N. Zhang, F. Liu, Z.-H. Wang, W.-Y. Zhu, G.-Z. Zhang, Z.-Y. Niu, X.-F. Wang and Z. Tan, *Journal of Alloys and Compounds*, 2021, **873**.

42. X. Wang, S. Xi, P. Huang, Y. Du, H. Zhong, Q. Wang, A. Borgna, Y. W. Zhang, Z. Wang, H. Wang, Z. G. Yu, W. S. V. Lee and J. Xue, *Nature*, 2022, **611**, 702-708.

43. W. H. Lee, M. H. Han, Y. J. Ko, B. K. Min, K. H. Chae and H. S. Oh, *Nat Commun*, 2022, **13**, 605.

44. Y. J. Wu, J. Yang, T. X. Tu, W. Q. Li, P. F. Zhang, Y. Zhou, J. F. Li, J. T. Li and S. G. Sun, *Angew Chem Int Ed Engl*, 2021, **60**, 26829-26836.

45. X. Zhao, Z. H. Levell, S. Yu and Y. Liu, *Chem Rev*, 2022, **122**, 10675-10709.

46. J. K. Nørskov, J. Rossmeisl, A. Logadottir, L. Lindqvist, J. R. Kitchin, T. Bligaard and H. Jónsson, *The Journal of Physical Chemistry B*, 2004, **108**, 17886-17892.

47. J. Gao, C.-Q. Xu, S.-F. Hung, W. Liu, W. Cai, Z. Zeng, C. Jia, H. M. Chen, H. Xiao, J. Li, Y. Huang and B. Liu, *Journal of the American Chemical Society*, 2019, **141**, 3014-3023.

48. H. B. Tao, L. Fang, J. Chen, H. B. Yang, J. Gao, J. Miao, S. Chen and B. Liu, *J Am Chem Soc*, 2016, **138**, 9978-9985.